

Dimming GRS 1915+105 observed with NICER and Insight–HXMT

M. Zhou¹, V. Grinberg², A. Santangelo¹, C. Bambi^{3,4}, Q. Bu⁵, C. M. Diez⁶, L. Kong¹, J. F. Steiner⁷, and Y. Tuo¹

¹ Institut für Astronomie und Astrophysik, Universität Tübingen, Sand 1, 72076 Tübingen, Germany
menglei.zhou@astro.uni-tuebingen.de

² European Space Agency (ESA), European Space Research and Technology Centre (ESTEC), Keplerlaan 1, 2201 AZ Noordwijk, The Netherlands

³ Center for Astronomy and Astrophysics, Center for Field Theory and Particle Physics, and Department of Physics, Fudan University, Shanghai 200438, China

⁴ School of Natural Sciences and Humanities, New Uzbekistan University, Tashkent 100007, Uzbekistan

⁵ Institute of Astrophysics, Central China Normal University, Wuhan 430079, China

⁶ European Space Astronomy Centre (ESAC), Camino Bajo del Castillo s/n, Villanueva de la Cañada, 28692 Madrid, Spain

⁷ Harvard-Smithsonian Center for Astrophysics, 60 Garden Street, Cambridge, MA 02138, USA

–/–

ABSTRACT

The black hole X-ray binary GRS 1915+105 was bright for 26 years since its discovery and is well-known for its disk instabilities, quasi-periodic oscillations, and disk wind signatures. We report a long-term spectral-timing tracing of this source from mid-2017 until the onset of the “obscured state”, based on the complete data from the Neutron Star Interior Composition Explorer (NICER) and the Insight—Hard X-ray Modulation Telescope (HXMT), whose hard coverage decisively informs the modeling at lower energies. In the soft state predating 2018, we observed highly ionized winds. However, in the hard state shortly before transitioning into the “obscured state” on May 14, 2019 (MJD 58617), the winds exhibited a discernible reduction in ionization degree ($\log \xi$), decreasing from above 4 to approximately 3. Our analysis involves the measurement of the frequencies of the quasi-periodic oscillations and the estimation of the properties of the ionized winds and the intensities of different spectral components through spectroscopy during the decay phase. We delve into the origin of these infrequently observed warm outflows in the hard state. It is found that the launching radius of the winds in the hard decay phase is similar to that in the soft state, indicating the launching mechanism of those winds in both states is likely the same. The presence of the ionized winds is preferentially dependent on the periphery of the accretion disk, but not directly related to the corona activities in the center of the binary system.

Key words. X-rays: binaries – Accretion, accretion disks – X-rays: individuals: GRS 1915+105 – Stars: black holes

1. Introduction

Black hole binaries (BHBs) consist of a black hole and a donor star companion (for a review on BH binaries, see e.g. [Remillard & McClintock 2006](#), and the references therein). The black hole (BH) accretes matter from its companion star. The accretion process leads to the release of intense radiation and outflows that can be observed across the electromagnetic spectrum. Among BHBs, GRS 1915+105 is particularly interesting. First discovered by the GRANAT/WATCH all-sky monitor in 1992 ([Castro-Tirado et al. 1992, 1994](#)), GRS 1915+105 has been well-studied. The captivating phenomena of this source – such as the exhibition of apparently superluminal radio jets ([Mirabel & Rodríguez 1994](#)), rarely-seen high-frequency quasi-periodic oscillation (HFQPO) features in the timing domain ([Morgan et al. 1997](#)), the highly-ionized winds generated from the accretion disk ([Lee et al. 2002; Ueda et al. 2009](#)), and the characteristic patterns of its light curves that can be classified into at least 14 different classes ([Belloni et al. 2000; Klein-Wolt et al. 2002; Hannikainen et al. 2005; Zoghbi et al. 2016; Athulya et al. 2022; Shi et al. 2023](#)), – all make GRS 1915+105 valuable and important to our understanding of astrophysical processes such as accretion, and the outflow formation including the jet ejection and disk winds.

Unlike other transient X-ray binaries that brighten and fade during weeks or months (e.g., [Remillard et al. 1999; Homan et al. 2001; Williams et al. 2020](#)), GRS 1915+105 was consis-

tently bright for 26 years since its discovery and was thought to be a quasi-persistent source. However, its luminosity unexpectedly underwent an exponential decay in early 2018 ([Negoro et al. 2018](#)). During this flux decline, the source also showed prominent and narrow low-frequency quasi-periodic oscillation (LFQPO) features ([Koljonen & Hovatta 2021](#)). It was then believed that GRS 1915+105 had nearly finished its 26-year-long outburst and entered its quiescent state. In April, 2019 (\sim MJD 58600), the source became dimmer during a pre-flare dip ([Homan et al. 2019](#)). A few days later, short flares lasting for hours were observed in both radio and X-ray band ([Motta et al. 2019, 2021; Koljonen et al. 2019](#)), but with an even lower average X-ray flux. The LFQPO features within 1–10 Hz were either halted or became undetectable synchronously. However, during a 60 days re-brightening phase in mid-2021, strong QPO features with an unprecedentedly low frequency ($f_{\text{QPO}} \approx 0.2$ Hz) were discovered ([Kong et al. 2024](#)). Intriguingly, despite the rapid luminosity decay measured in X-rays, the radio observations suggest that GRS 1915+105 remains active in the accretion process after mid-2019.

Generally, the physics of the state transition of BHBs are not fully understood. Empirically, a typical outburst observed in a BHB can form a q-track in its hardness-intensity diagram (HID) ([Homan et al. 2001; Fender et al. 2006](#)). During the hard state in which the (cut-off) power-law emission dominates in X-

rays, jet emission is observed in radio/infrared bands and LFQPOs in the timing domain often emerge. In contrast, in the soft state when thermal radiation becomes primary, the jet typically becomes either weak and unstable or undetectable, with a power spectrum dominated by flicker noise. The central frequencies of the LFQPOs are found to have a negative correlation with the spectral hardness up to at least 90 keV (e.g., [Zdziarski et al. 2004](#); [Soleri et al. 2008](#); [Zhou et al. 2022](#)). As an ingredient involved in the accretion process, ionized disk winds are believed to play an important role during the state transition and are preferentially discovered in the soft state where the jet emission is usually quenched ([Neilsen & Lee 2009](#); [Ponti et al. 2012](#)). The state-dependent anti-correlation between the disk winds and the jets indicates that the disk winds may work as an alternative mode to eject matters. Former studies have shown that GRS 1915+105 displays prominent blue-shifted ionization absorption features, e.g., the Fe xxv He α line and Fe xxvi Ly α line, located at 6.7 keV and 7 keV, respectively ([Ueda et al. 2009](#); [Miller et al. 2016](#); [Neilsen et al. 2018](#)).

The mechanism driving the ionized absorption outflow is still unclear. It can be generated by radiation pressure if the luminosity of the source approaches the Eddington limit ([Proga & Kallman 2002](#); [Higginbottom & Proga 2015](#)), thermal pressure when the gas of the disk atmosphere is irradiated by the energetic photons from the inner part of the accretion disk ([Begelman et al. 1983](#); [Woods et al. 1996](#); [Done et al. 2018](#)), or magnetic pressure given a strong magnetic field close to the BH ([Fukushima et al. 2017](#)). Additionally, the partial concealment of cold dense absorption detected in some BHBs may also arise from an internal obscured clump that failed to escape from the strong gravitational field ([Miller et al. 2020](#)). The presence of the obscured clump, exhibiting fast absorption variabilities that can be seen in BHBs (see e.g., [Motta et al. 2017a,b](#); [Koljonen & Tom-sick 2020](#); [Balakrishnan et al. 2021](#)) and active galactic nuclei (AGNs) (e.g., [Matt et al. 2003](#)), provides significant diagnostic information to understand how accretion behaves within a full range of BH masses from a few M_{\odot} to $10^9 M_{\odot}$.

In the present paper, we focus on the period just before GRS 1915+105 entered the “obscured” state, using all the public data observed between MJD 57932 (June 8, 2017) and MJD 58608 (May 5, 2019), which are obtained from the archive of NICER/XTI and Insight–HXMT. We perform a spectral-timing analysis based on these data, tracing the evolution of key parameters and probing their correlations using the simultaneous broad-band coverage by both instruments, in particular, the high energy coverage afforded by HXMT where available, to inform also the single-instrument fits. The results contribute to understanding the physics of the accretion process and the mechanisms behind the state transitions of transient BHBs. The remainder of this paper is structured as follows: in Sect. 2, we present the long-term behaviors of the source and an overview of the data we analyze in this paper. The spectral-timing analysis is detailed in Sect. 3 and the results are presented in Sect. 4. We discuss the results of our analysis in Sect. 5. A summary and outlook are presented in Sect. 6.

2. Observations and Data Reduction

The long-term behavior of GRS 1915+105 since 2017 is shown in Fig. 1. The light curve monitored by MAXI ([Matsuoka et al. 2009](#)) indicates that this source was consistently active before 2018 but then underwent a transition from an exponential decay to a linear decay till the beginning of May 2019 (here we follow the state definitions in [Koljonen & Hovatta 2021](#)). Whereafter,

the source became extraordinarily faint, with its flux reduced by a factor of 10. It exhibited three month-long flares and several short flares lasting only a few hours in the X-ray band (see e.g., [Neilsen et al. 2020](#); [Kong et al. 2021](#)), but it remained particularly active in the radio band ([Motta et al. 2021](#)). Thanks to the abundant observations focusing on GRS 1915+105 by NICER and HXMT, we can trace this source’s evolution closely after 2017. Here, we are particularly interested in the observations before the source entered the purely obscured state, utilizing all the available NICER and HXMT data before MJD 58617.

Both the X-ray Timing Instrument (XTI) of the Neutron Star Interior Composition Explorer (NICER, [Gendreau et al. 2016](#)) and the Insight–Hard X-ray Modulation Telescope (Insight–HXMT or HXMT, [Zhang et al. 2014, 2020](#)) produce impactful spectral-timing data. The XTI consists of an aligned collection of 56 X-ray “concentrator” optics and silicon drift detector pairs, extending to a softer X-ray band (0.25–10 keV) with a time-tagging resolution of ~ 100 nanoseconds. HXMT instead has a broader energy band ranging nominally from 2 to around 250 keV, realized by three collimated telescopes: the Low-Energy (LE) telescope, whose energy range covers the 1–15 keV band ([Chen et al. 2020](#)); the Medium Energy (ME) telescope, covering 5–30 keV ([Cao et al. 2020](#)); and the High Energy (HE) telescope, covering the 25–250 keV band ([Liu et al. 2020](#)). In particular, the fast temporal response and large effective area of HXMT at higher energies, allow us to conduct spectral-timing studies above 15 keV and in particular to better constrain the continuum spectral models by providing high energy leverage on spectral shape. We present the details of the data processing in the following subsections.

2.1. NICER data

We process all NICER data using tools provided in HEASOFT v6.32.1 and the calibration database xti20221001. The cleaned event lists are produced by the standard nicerl2 task, including calibration and filtering steps. To minimize the background effects, we apply a custom set of selection criteria to identify good time intervals (GTIs) based on standard NICER screening criteria: overshoot rate less than 10 cts per FPM (FPM_OVERONLY_COUNT<10), undershoot rate less than 200 cts per FPM (FPM_UNDERONLY_COUNT<200), and geomagnetic cutoff-rigidity greater than 2 GeV (COR_SAX>2). The photons registered by the noisy detectors (DET_ID=14, 34, 43, 54) are also omitted (e.g., [Bogdanov et al. 2019](#)). Finally, we extract the spectra and light curves within our selected GTIs with nicerl3-spect and nicerl3-1c. The background spectrum is estimated with model 3C50 ([Remillard et al. 2022](#)). The noticed energy band for the spectral analyses is 0.4–10 keV.

2.2. HXMT data

For the HXMT data, we use the pipeline based on Insight–HXMT Data Analysis Software (HXMTDAS) v2.05 and the calibration database v2.06. The GTIs are selected according to the following criteria: elevation angle larger than 10° (ELV>10), geomagnetic cut-off rigidity larger than 8 GeV (COR>8), offset angle from the pointing direction smaller than 0.04° (ANG_DIST<0.04), and at least 300 seconds before and after the South Atlantic Anomaly passage (T_SAA>=300 && TN_SAA>=300). We adopt an additional criterion for the LE telescope: the elevation angle for the bright Earth is larger than 30° . Since the individual detectors of the HXMT instruments have

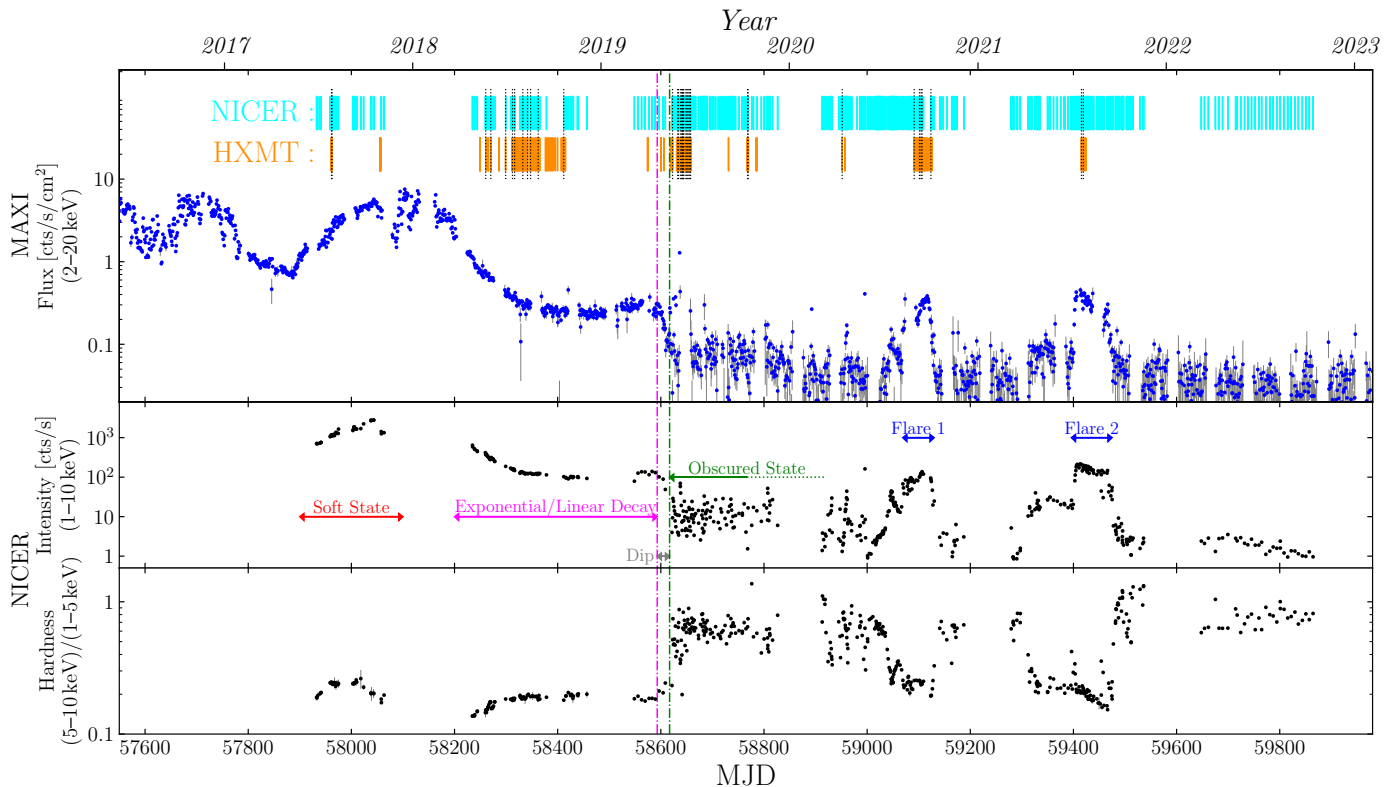


Fig. 1. Long-term behavior of GRS 1915+105 monitored by MAXI and NICER. Top panel: the daily flux measured by MAXI in the 2–20 keV band. The duration of NICER and Insight–HXMT observations is shown at the top with cyan and dark orange stripes. We use black dotted lines to denote the available quasi-simultaneous observations by two instruments. Middle panel: the intensity of GRS 1915+105, defined by the raw photon count rate registered in the 1–10 keV band of NICER. The spectral states are classified with spectral-timing features and denoted with arrows. More details can be found in the literature. Bottom panel: the hardness of the spectra, defined by the raw count rate between the 5–10 keV band and the 1–5 keV band of NICER. We use a magenta vertical dash-dotted line (\sim MJD 58593) to represent the start point of the pre-flare dip and a green dash-dotted line (\sim MJD 58617) to mark the pass of this source into the obscured state.

different fields of view (FoVs), we selected photon events registered by detectors with a small FoV for the following analysis.

The energy bands for the spectral analyses are 2–10 keV for LE, 10–30 keV for ME, and 28–90 keV for HE. We additionally ignore photons within the 21–24 keV band of the ME telescope to avoid detecting the silver K-shell fluorescent lines produced by the material of the instrument (Li et al. 2020). We use the tools LEBKGMAP (Liao et al. 2020a), MEBKGMAP (Guo et al. 2020), and HEBKGMAP (Liao et al. 2020b) provided by the HXMT team to estimate the instrumental background.

2.3. Joint fitting with both NICER and HXMT data

NICER has a large effective area in the soft X-ray band (~ 1900 cm² peaking at 1.5 keV), making it well-suited for probing absorption characteristics, while HXMT covers a wider energy range up to roughly 250 keV, enabling a good constraint on the slope of the continuum. We aim to capitalize on the combination of both X-ray missions where simultaneous data is available and use the results to inform models where only coverage below 10 keV exists allowing improved modeling and better model constraints. We have a total of 20 joint spectra before the obscured state of GRS 1915+105 (see the top panel in Fig. 1). Among these, 7 occurred before 2018 (in the soft state) and 13 during the exponential/linear decay during which the spectra are relatively hard. We can optimize our modeling by conducting joint fitting, helping rule out unsound parameters and obtain better constraints on various theories. We utilize both NICER/XTI

and HXMT/ME to extend our spectra to higher energies for observations prior to 2018, as HXMT/HE is predominantly affected by background. During the decay phase, we combine the spectra from NICER/XTI, HXMT/ME, and HXMT/HE.

3. Spectral-timing analysis

We use ISIS v1.6.2 (Houck & Denicola 2000) —which allows access to the defined models in Xspec (Arnaud 1996)—to perform the spectral-timing fitting.

3.1. Timing analysis

All the light curves obtained from both NICER and HXMT are directly generated from the corresponding screened event lists, processed with Stingray (Bachetti et al. 2021; Huppenkothen et al. 2019a,b). The selected energy range for NICER/XTI is 1–10 keV. The time resolution (Δt) of these light curves is set to 2^{-9} s \approx 2 ms. The power spectrum densities (PSDs) are computed using segments with a length of $2^{14} \times \Delta t = 32$ s. Thus, the Nyquist frequency for those PSDs is $f_{\max} = 1/(2\Delta t) = 256$ Hz and the lowest frequency we can access is $f_{\min} = 1/(n_{\text{bins}}\Delta t) = 0.03125$ Hz. The frequencies f are rebinned logarithmically between f_{\min} and f_{\max} , with an equally spaced grid in logarithmic scale $df/f = 0.03$. The expectations of the white noise are reduced according to Zhang et al. (1995). We omit the data above 30 Hz since they are Poisson-noise dominated.

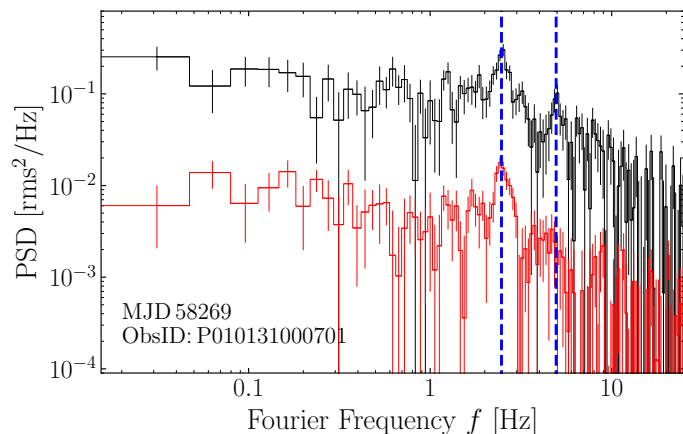


Fig. 2. Typical PSDs observed with HXMT/LE (in black) and HXMT/ME (in red) simultaneously. The PSDs of LE are multiplied by a constant of 20 to avoid overlapping in the figure. The central frequencies of the main QPO and its first harmonic are 2.47 Hz and 4.94 Hz, respectively, indicated by two dashed blue lines.

The spectral states of GRS 1915+105 can be classified clearly by the timing properties. Before 2018, GRS 1915+105 was in a spectrally soft state, with its light curve categorized predominantly as the class λ (Belloni et al. 2000; Neilsen et al. 2018). The flicker noise dominated the power spectrum, without unambiguous LFQPO features shown in the 1–10 Hz band. From the end of April 2018 to the end of April 2019, the power spectra exhibited at least two prominent LFQPO features whose central frequencies were in the 1–10 Hz range. At the end of the decay phase, the power spectra were dominated by Poisson noise since MJD 58621 (May 18th, 2019), marking the onset of the obscured state. During the year before the onset of the obscured state, we additionally examine the data from HXMT/LE and HXMT/ME, finding that the central frequencies of the LFQPO components are consistent in those simultaneous observations (see e.g., Fig. 2), despite the noisier PSDs produced by HXMT than NICER’s due to HXMT’s stronger background effects. The QPOs thus clearly extend above 10 keV, i.e. in a range that is dominated by the continuum with no disk contribution.

We model the NICER spectra as they are less affected by noise choosing an empirical model consisting of two Lorentzian functions with central frequencies fixed at zero to characterize the noise continuum (Nowak 2000). The combination of these two Lorentzians is appropriate for both flicker noise and flat-top noise with a high-frequency cut-off. The LFQPO signals are captured by three additional Lorentzian functions with free central frequencies. Two typical fits with this model are shown in Fig. 3. We can obtain a relatively good fit for most of our power spectra. The most significant Lorentzian signal with a lower frequency is identified as the main QPO component, and the second with a higher frequency is recognized as the first harmonic. We show their central frequencies along with their posterior uncertainties versus time in Fig. 4, and the correlation between those two components in the upper panel of Fig. 6. Our findings suggest that there is always a 2:1 relationship between the central frequencies of two QPO components, which measures LFQPO frequencies more soundly. While we occasionally observe a third QPO component, there are no clear patterns in its appearance concerning the former two prominent QPO features.

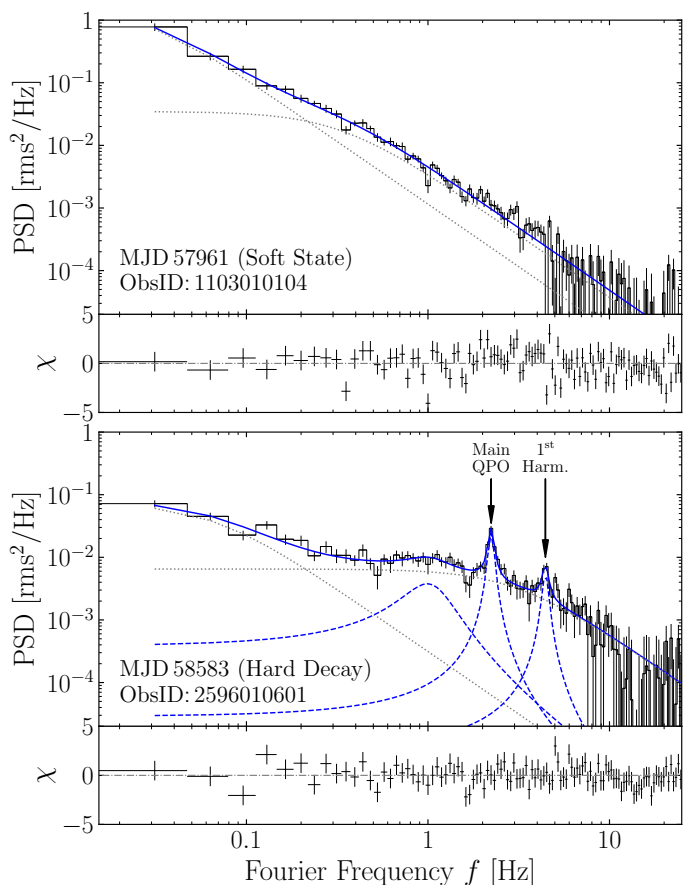


Fig. 3. Two typical power spectra produced by NICER data in the soft state (upper panel) and the hard state during the decay phase (lower panel), respectively, with their best-fit models. The Lorentzians with a central frequency at zero are indicated with grey dotted lines, and the Lorentzians with a non-vanishing central frequency are indicated with blue dashed lines. As the best-fit model, the sums of all the Lorentzians are denoted with solid blue lines. The measured central frequencies of the main QPO and the first harmonic in the hard state are $2.23^{+0.18}_{-0.19}$ Hz and $4.44^{+0.05}_{-0.06}$ Hz, respectively.

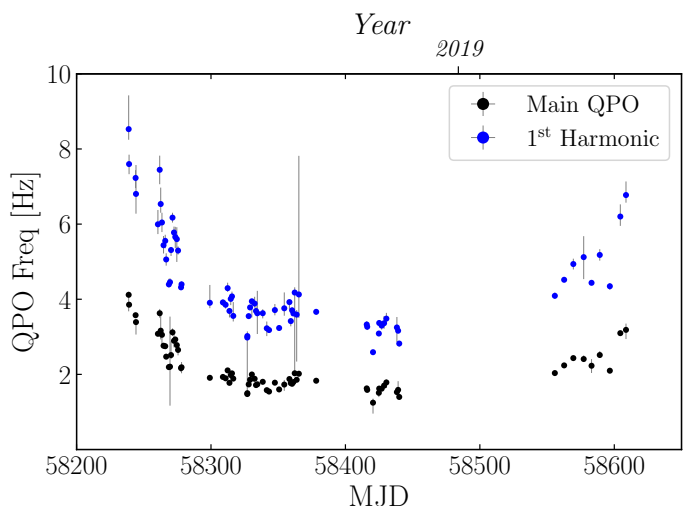


Fig. 4. The evolution of the QPO frequencies versus time during the exponential/linear decay. We observe a clear long-term evolution of the state, with first decreasing and then increasing central frequencies of the main QPO and its harmonic.

3.2. Spectral analysis

We adopt a systematic error of 0.5% and 1.0% for HXMT/ME and HXMT/HE respectively (Li et al. 2020), and of 1.5% for NICER/XTI¹. All the spectra are grouped using the optimal binning method detailed in Kaastra & Bleeker (2016), with a minimum of 30 photon counts per bin ensured.

3.2.1. Preliminary modeling for NICER only

We first try to fit the NICER spectra with a simple continuum of the Comptonization emission produced by the corona (Nthcomp, Zdziarski et al. 1996; Życki et al. 1999), multiplied by the galactic absorption model TBabs to characterize the photoelectric absorption by the interstellar medium (ISM). The cross-sections are provided by Verner et al. (1996) and the element abundances are given by Wilms et al. (2000). The multi-temperature thermal radiation generated from the accretion disk (diskbb, Mitsuda et al. 1984; Makishima et al. 1986) is further included in our model in the soft state. Typical residuals are presented in the upper panel of Fig. 5. These exploratory fits are usually bad with high reduced χ^2 s, but we can obtain a well-constrained estimation of the photon index of the continuum. The correlation of the main QPO frequencies and the measured photon index Γ is shown in blue in the lower panel of Fig. 6. A quasi-linear trend between these two parameters is observed even with this preliminary model.

In the soft state, we detect absorption at ~ 7 keV that we identify with Fe xxvi Ly α . The observed Fe K α emission line is broadened.

During the decay phase, we detect a narrow emission feature below 7 keV. This feature plays a major role in shaping the whole iron line region of the spectrum. If one assumes that this narrow iron line is produced from the accretion disk and models the region with a single relativistic reflection model, the inferred inclination angle of the system will be less than 30° (see, e.g., Table 4 in Shreeram & Ingram 2020), in contradiction to known constraints on the inclination of GRS 1915+105 to be in the order of $i \simeq 60^\circ$ (e.g., Reid et al. 2014; Fender et al. 1999). If we constrain the inclination angle in our model to 60° , the iron line region, particularly the narrow component, cannot be well modeled. Therefore, we conclude that an additional component, a distant reflector, is necessary, and the observed complexity of the iron line region is an interplay of the broad relativistic and narrow distant components.

Aside from the narrow iron line, one unsolved feature remains in the residual plots—a suspected extra Si edge at ~ 1.84 keV. This extra Si edge has been discussed in e.g., Lee et al. (2002), Martocchia et al. (2006), and Koljonen & Hovatta (2021), and is likely attributed to calibration issues. To consider this additional absorption edge, we add an edge model whose threshold energy is fixed at 1.84 keV, multiplying across the entire model.

So far, we have a simple phenomenological model for GRS 1915+105 in both the soft and hard states. However, more interesting information on the accretion system can be extracted from the spectra if an improved physical model is used. We will introduce an improved model for spectral fitting in the next section, where we use both NICER and HXMT data to constrain the broadband shape of the continuum.

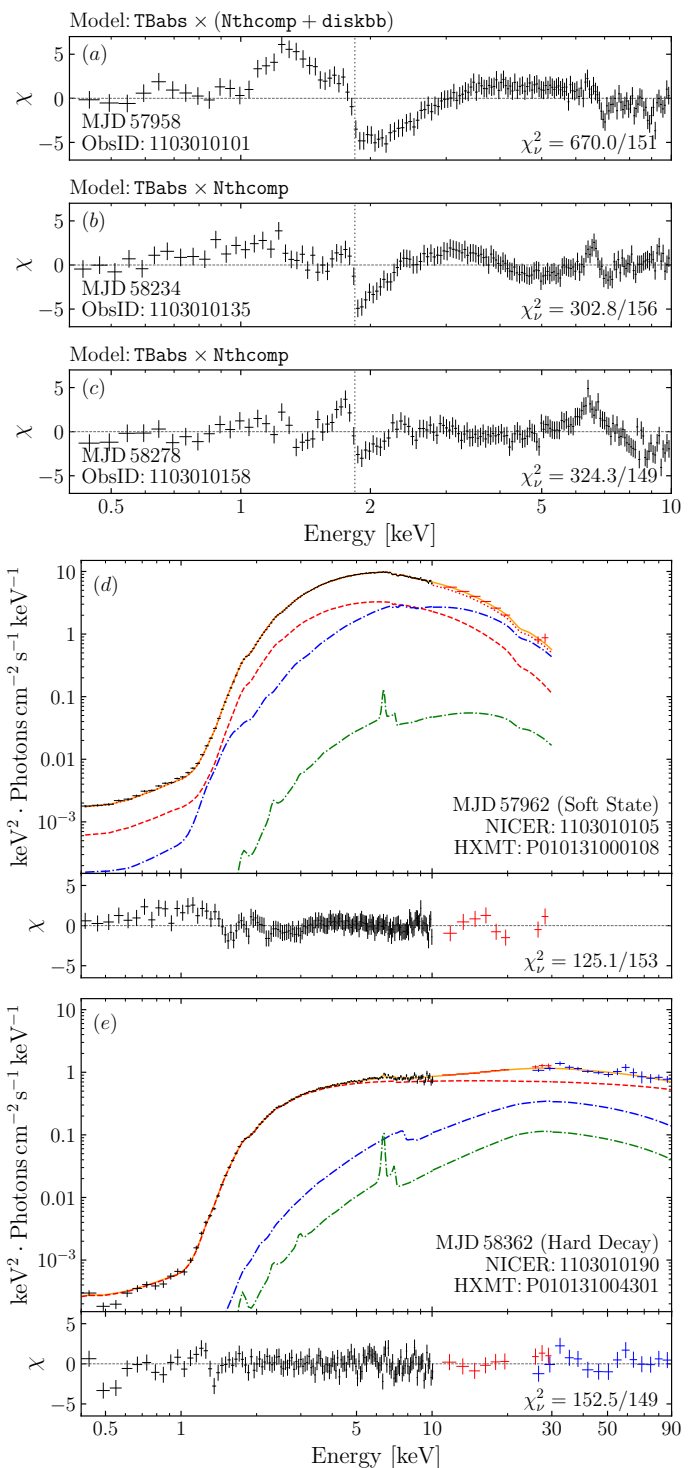


Fig. 5. From (a) to (c): Residuals to preliminary modeling fitting the NICER observation during the soft state (MJD 57958), at the beginning and the middle of the decay phase (MJD 58234 & 58278). We can see an additional silicon absorption edge (1.84 keV, denoted by a dotted line) and a narrow iron K α line with its cut-off energy of less than 7 keV. From (d) to (e): Two typical merged unfolded spectra of GRS 1915+105 in different states, fit by the physical model illustrated in Eq. 1. Different spectral components, i.e., the power-law continuum, the relativistic reflection component from the accretion disk, and the non-relativistic reflection component from a distant reflector, are shown with the red dashed line, the blue dash-dot line, and the green dash-dot line, respectively. Please refer to the text for detailed information.

¹ https://heasarc.gsfc.nasa.gov/docs/nicer/analysis_threads/cal-recommend/

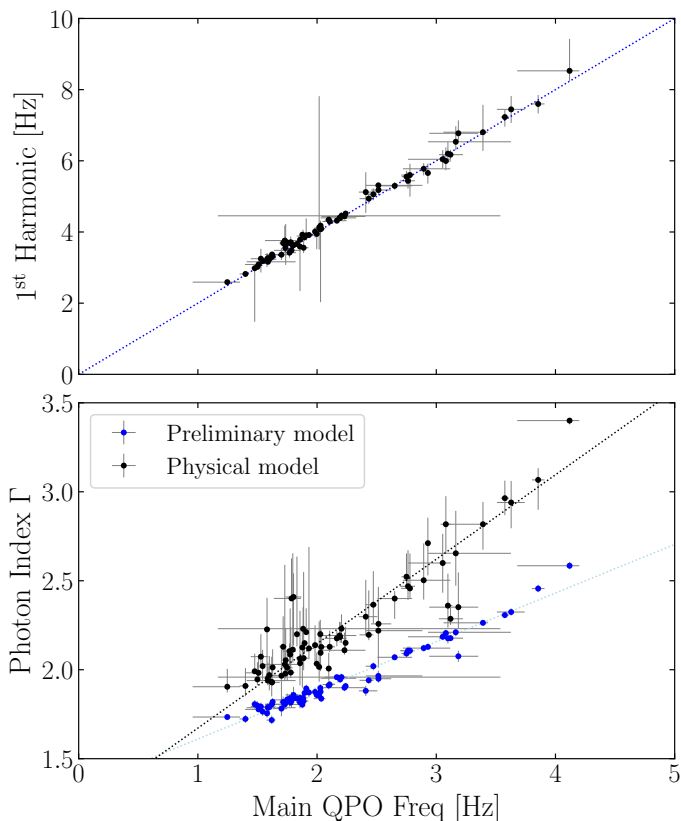


Fig. 6. Upper panel: the correlation between the main QPO frequency and the first harmonic. The dotted blue line indicates the double relationship. Lower panel: the correlation between the main QPO frequency and the measured photon index Γ with a preliminary model and an improved physical model described in Sect. 3.2.1 and 3.2.2, respectively. The dotted lines show the best fits assuming a linear model.

3.2.2. An improved physical model for simultaneous fitting

We start the joint fitting with both NICER and HXMT data to construct an improved physical model for both the soft state before 2018 and the dimming phase after 2018 of GRS 1915+105. Due to the broader energy coverage when using both instruments, some key parameters, e.g. the photon index Γ and the intensity of the reflection component can be better constrained by the joint modeling.

Based on the results provided by our preliminary fitting in Sect. 3.2.1, we use Comptonization continuum multiplied by a neutral absorption model TBabs. We consider an additional Si absorption edge and a non-relativistic reflection component as our initial improvement. We choose `xillverCp` to characterize this distant reflector (García et al. 2013).

With the distant reflector, we still have to consider the effect of the accretion disk. We use a fully relativistic reflection model `relxillCp` (from the `relxill` v2.3 package) to model the reflection produced on the accretion disk (García et al. 2014; Dauser et al. 2014). The indices of the emissivity profile q_{in} and q_{out} are fixed at 3, assuming the flat spacetime. The BH's spin a_* is fixed at 0.98 (Miller et al. 2013; Reid et al. 2014) and the inclination angle is fixed at 60° (Reid et al. 2014; Fender et al. 1999). We freeze R_{in} at the innermost stable circular orbit (ISCO). The outer radius of the disk is fixed at $400 r_g$, which can be considered sufficiently large. The indices of the power-law Γ and the temperatures of the electrons kT_e in both `relxillCp` and `xillverCp` are linked together with the parameters in the

`Nthcomp` model because we assume the incident spectrum for both reflectors is the same. The elemental abundance of the iron A_{Fe} in both reflection models are tied and we first allow it to vary between 0.5 and 2 in units of solar abundance. The ionization degrees $\log \xi$ and the electron densities $\log N$ in `relxillCp` and `xillverCp` are freed, as we cannot presume the properties of the reflectors at this stage. We set `refl_frac=-1` in both two reflection models, so only the reflection fraction of the `relxillCp` and `xillverCp` is taken into account. Since both `relxillCp` and `xillverCp` are calculated with the inner temperature of the seed photons produced by the disk fixed at 0.01 keV, we use a multiplicative table model `nthratio`² to correct their slope in the low energy band.

We select the table model `zxcipcf` to characterize the ionization absorption lines, and it provides a rough estimate of the ionization degree (Reeves et al. 2008). We note that `zxcipcf` is calculated based on XSTAR (Kallman et al. 2004), whose elemental abundances are given by Grevesse et al. (1996) that are different from Wilms et al. (2000). In addition, the absorption features are calculated with a given ionization degree $\log \xi$ with the assumption that the source has an initial power-law spectrum of $\Gamma = 2$. So if the spectrum heavily deviates from a $\Gamma = 2$ power-law, the estimated ionization parameter will be unreliable, especially when the ionization parameter is required for further physical calculations. Nevertheless, considering all these caveats, this model is still our best choice, as it is fast and universal for absorption from cold to hot plasma. We fix the covering fraction of `zxcipcf` at 1 and freeze the red-shift factor at 0, as the wind velocity cannot be constrained well due to the gain calibration of NICER.

In Xspec parlance, the full model used in the following spectral analysis can be written as

$$\text{TBabs} \times \text{edge} \times \text{zxcipcf} \times (\text{Nthcomp} + \text{diskbb}) \\ + \text{nthratio} \times (\text{relxillCp} + \text{xillverCp}). \quad (1)$$

We note that the spectra do not show strong ionized absorption features in 2018 when the source was in the decay phase. Therefore, we omit the `zxcipcf` component in Eq. 1.

The NICER-only observations have been previously analyzed by Koljonen & Hovatta (2021). Our model is developed using the HXMT data to constrain the continuum above 10 keV and while it is similar to the one employed in Koljonen & Hovatta (2021), it shows several differences. First, we opt for TBabs combined with an additional Si edge to minimize the impact of the absorption model on the slope of the continuum. We incorporate emission lines from various elements using `xillverCp` and account for the absorption lines with `zxcipcf`, to accurately estimate the ionization degree and the flux ratios among different spectral components. Finally, we employ `nthratio` to adjust the slopes of the reflection components, ensuring consistency with the incident spectrum.

We show examples of the joint results that fit with this optimized modeling in the panel (d) and (e) in Fig. 5. We obtain better fit statistics than with the preliminary model, and almost all features in the residuals vanish. The fits show that the iron abundance A_{Fe} and the electron density $\log N$ in `xillverCp` cannot be constrained in most of our observations, so later we fix A_{Fe} at the solar value and set $\log N$ to 15. The ionization degree of `xillverCp` is also fixed at the lowest value ($\log \xi = 0$) as a cold distant reflector is assumed.

² <https://github.com/garciafederico/nthratio>

3.2.3. NICER-only modeling

The joint fitting shows that the obtained temperature of the electrons kT_e reaches the upper limit of the allowed range (150 keV) in the decay phase. While in the soft state, the kT_e cannot be constrained even if the HXMT data are included. We free the electron temperature when fitting the data before 2018. As mentioned before, we omit the ionized absorption `zxcipcf` for the observations from MJD 58200 to MJD 58500. Therefore, we only consider the ionized absorption for the observations in the soft state (before 2018) and at the end of the decay phase (after 2019). The thermal emission from the disk—the `diskbb` component—is omitted during the decay phase, as the spectral fits suggest that the thermal emission is unnecessary.

For most of our observations, simultaneous NICER and HXMT data are not available. We base the fits to NICER-only data on the model developed above for the broader NICER + HXMT energy range with the following adaptations: we fix the kT_e at 150 keV in the hard decay phase, but free it in the soft state. The iron abundance A_{Fe} and the electron density $\log N$ of the distant reflector are fixed at the solar value and 15, respectively. The ionization degree $\log \xi$ of `xillverCp` is fixed at 0. The results of our fitting based on the NICER data are reported in Fig. 7.

4. Results

4.1. Before 2018

GRS 1915+105 was in the soft state, where thermal emission dominated the spectrum. The column densities N_{H} of the absorption caused by ISM is steadily measured at $(5.7 \pm 0.1) \times 10^{22} \text{ cm}^{-2}$. The Comptonization exhibits photon indices approaching the upper limit of our model ($\Gamma \simeq 3.4$), and the inner temperatures T_{in} of the accretion disk are approximately 1 keV, which are higher than those during the decay phase (see panel *a*, *c*, and *d* of Fig. 7). The electron temperatures kT_e are poorly constrained in the soft state, with a lower limit established at 5 keV. The accretion disk is highly ionized and the ionization degree $\log \xi$ is always greater than 3.

Our estimated T_{in} , which is $\simeq 1$ keV, is lower than previous studies (e.g., Neilsen et al. 2018 obtained a T_{in} of 1.65–2.15 keV based on the same NICER data). This is likely due to the lower estimation of the column density of the ISM absorption with our modeling.

The ionized absorption feature is detected in all the NICER observations before 2018. The material is highly ionized with an ionization degree ($\log \xi$) greater than 4. The dips produced by the ionized absorption shown in the spectra are mostly the Fe xxv Ly α line at 7 keV (see panel *a* of Fig. 5). The column densities of the absorption are poorly constrained as the winds are highly ionized.

Here we use the formula $R_{\text{launch}} \leq \sqrt{L/(N_e \cdot \xi)}$ to estimate the upper limit of the launching radius of the winds, where L is the unabsorbed luminosity of the source (Tarter et al. 1969). The unabsorbed luminosity of the source keeps at $\sim (18 \pm 8)\% L_{\text{Edd}}$ in the soft state before 2018. The electrons' number density N_e of the winds is typically quoted as 10^{14} cm^{-3} (following the method described in Sect. 4 of Neilsen et al. 2020). The estimated launching radius with the fixed electron density is 10^3 – $10^4 r_g$ and significantly shows a negative correlation with the ionization degree. The results are shown in Fig. 8. We do not see a strong correlation between R_{launch} and the disk inner temperature T_{in} .

4.2. During the decay phase

With the modeling described in Sect. 3.2, we obtained fruitful results from the spectral analysis focusing on the exponential/linear decay phase. The behaviors of the source can be traced via the evolution of the key parameters.

4.2.1. The QPO- Γ correlation

We have illustrated the correlation between QPO- Γ and a preliminary model in Fig. 6. In the same figure, we also present their correlation with the improved physical model (Eq. 1) shown in black. The uncertainties of the newly estimated Γ are larger as the model becomes more complex and has more degrees of freedom. We notice that the new Γ values are consistently higher than those measured with the preliminary model. This is because the prominent iron line feature is absorbed in a continuum produced by the reflection process of an incident Comptonization spectrum, making the slope of the primary emission steeper. The quasi-linear correlation between the main frequency of the QPOs and the photon index is still maintained.

The evolution of the LFQPO central frequencies in Fig. 4 suggests that GRS 1915+105 begins in an intermediate state, transitions to a harder state since MJD 58200, and returns to a hard-intermediate state at the end of the decay phase. The photon index Γ of the Comptonization is mostly consistent with such a “canonical” state transition behavior. Although the strong ionized winds are detected at the end of the decay phase, the photon index values increase simultaneously with the frequencies of the QPOs. This phenomenon indicates that the corona behaves independently from the ionized disk winds. Instead, the QPO frequencies are strongly related to the corona.

The general quasi-linear correlation between the main QPO frequency and the photon index Γ of the power-law component is commonly seen in most BHBs, e.g., Cyg X-1, GX 339–4, 4U 1630–47 (see e.g., Tomsick & Kaaret 2000; Zdziarski et al. 2004; Motta et al. 2011; Böck et al. 2011; Grinberg et al. 2014; Zhou et al. 2022). Although fruitful theories have been proposed to physically explain the origin of QPOs, e.g. the Lense-Thirring precession (Bardeen & Petterson 1975; Ingram et al. 2009; Ingram & Done 2011) or the accretion-ejection instability (Tagger & Pellat 1999), where a large fraction of them assuming a truncated disk with hot flows inside, we cannot verify these theories by our results owing to the fixed inner radius of the accretion disk at ISCO in our model.

4.2.2. The ionization degree and the electron density of the accretion disk

Generally speaking, the influence of the ionization degree acting on the spectrum is complex. Different types of ions can produce large amounts of emission lines depending on the abundance of ions. These emission lines are broadened due to the general relativistic effects and the reflection spectrum is partly smoothed in the soft X-ray band. However, the iron emission lines at 6–7 keV are usually not strongly affected by other emission lines as iron is more abundant than other heavier elements. The ionization degree can be precisely measured with a clear cut-off energy of the iron line shape and a fixed inclination angle.

At the beginning of the decay phase, the ionization degree ($\log \xi$) is in the range of 2.7–3.0, close to the values we have seen in the soft state. However, shortly after the start of the decay phase (since MJD 58238), we observe two branches of potential solutions with distinct ionization degrees and comparable sta-

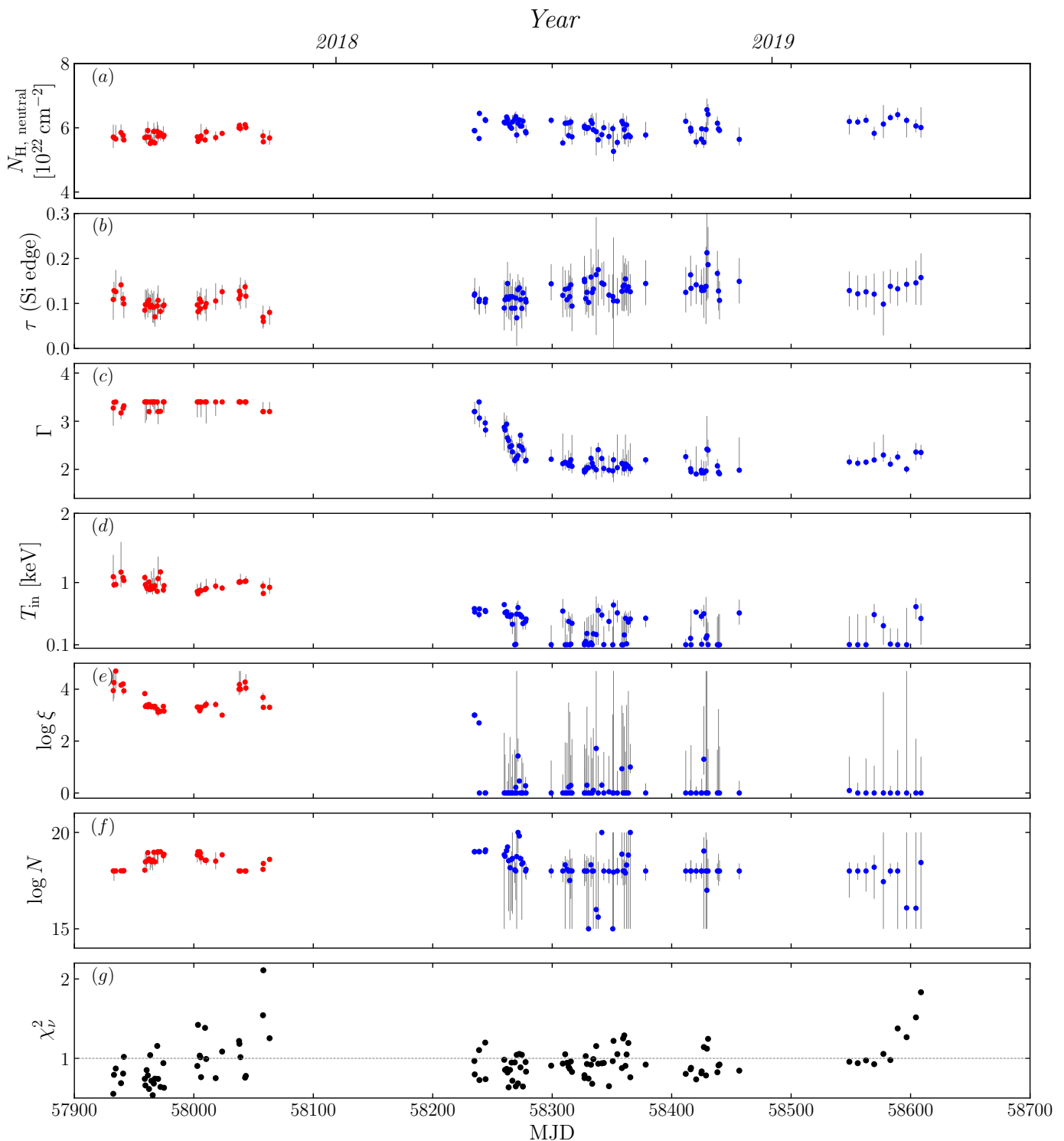


Fig. 7. Evolution of the key parameters measured via the spectral analysis as a function of time. The panels show (from a to g): the equivalent hydrogen column N_{H} of the neutral absorption, the optical depth τ of the extra silicon edge, the photon index Γ , the temperature at the inner edge of the disk T_{in} , the ionization degree $\log \xi$ of the accretion disk, the logarithmic number density of electrons of the accretion disk $\log N$, and the reduced chi-squares χ_{ν}^2 of the best-fits. Red and blue dots denote parameters obtained in the soft state and hard decay phase, respectively.

tistical significance based on spectral analysis. One example is shown in Fig. 9. One branch of solutions has very low ionization degrees ($\log \xi \leq 2$), with the relative intensities of the relativistic reflection component divided by those of the primary emission from the corona being higher. The other branch typically exhibits a high ionization degree ($3 \leq \log \xi \leq 4$), but the fluxes from the primary emission tend to vanish in most of the spec-

tra, causing the “reflection fraction” to approach an extremely high value, significantly greater than 10. Neither branch of solutions is universally superior to the other in a statistical sense. The strong degeneracy between the ionization degree and the relative intensity of spectral components arises from the asymptotic convergence between the reflection spectrum and the incident spectrum at high ionization degrees, where the material becomes

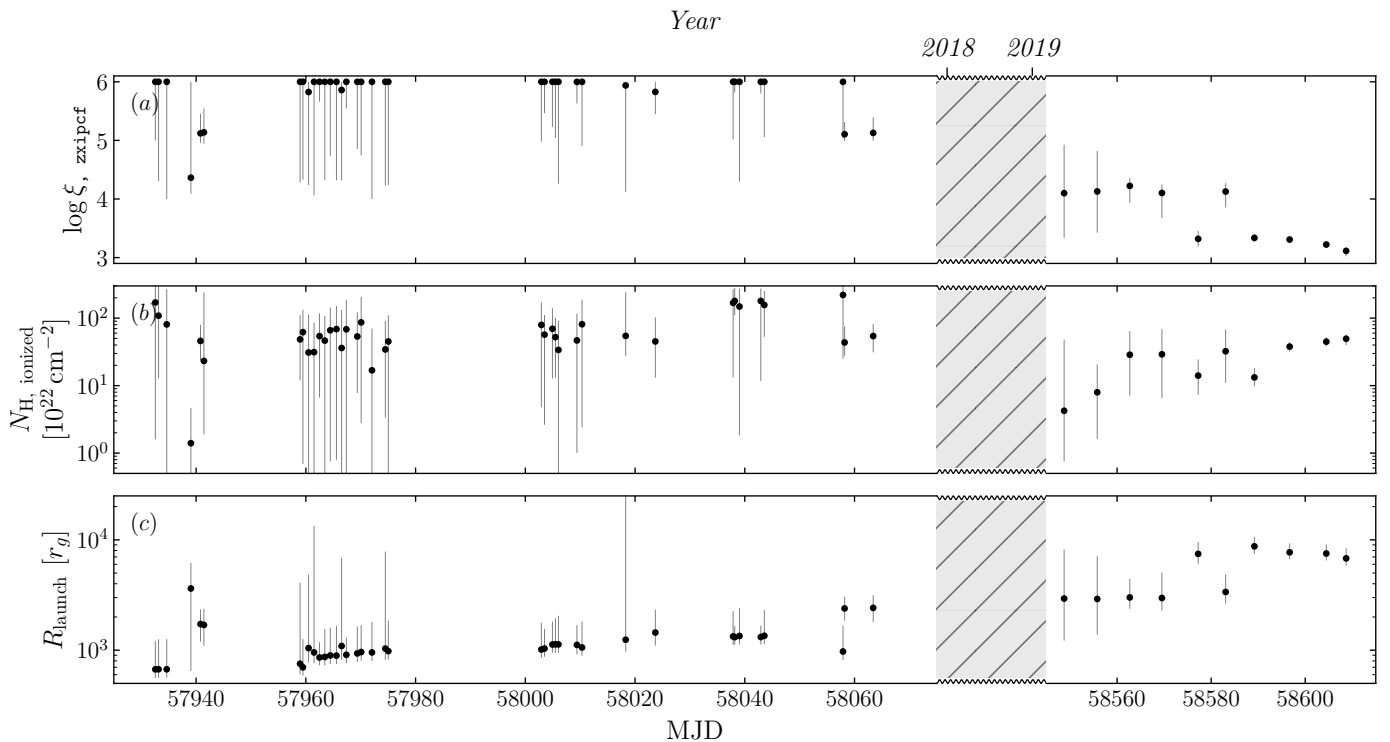


Fig. 8. The evolution of the ionized wind absorption feature in the soft state and near the end of the decay phase. We omit the period from MJD 58075 to 58545 as there is no strong evidence of an ionized absorption within this period. Panel (a): the ionization degree of the ionized absorption. Panel (b): the column density of the ionized absorption. Panel (c): The inferred launching radius of the ionized winds versus time given a typical number density of the winds of 10^{14} cm^{-3} .

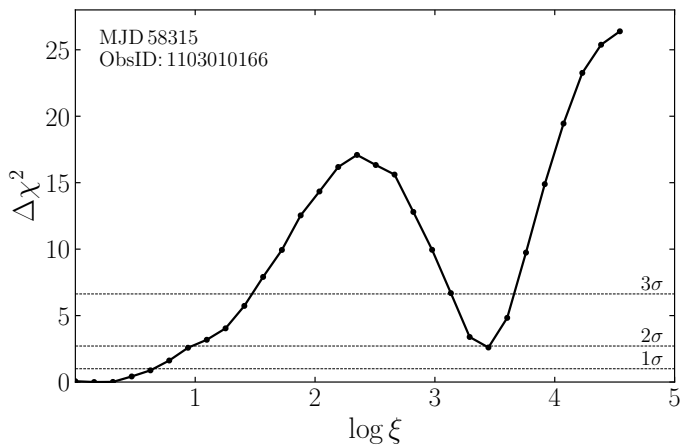


Fig. 9. $\Delta\chi^2$ fitting statistics of an example spectrum in the decay phase, plotted versus different values of the ionization degree $\log \xi$ of the relativistic reflection component `relxillCp`. The sample points are shown in black dots and connected by solid lines. There are two local minima in this plot, with distinct ionization degrees. In our work, we discard the solution with higher $\log \xi$ because it will result in a vanishing primary emission originating from the corona.

transparent to X-ray photons. Statistically, both branches of solutions should be retained. However, the strong LFQPO features observed in the time domain indicate that the primary emission from the corona should not be too weak. Therefore, we decide to discard the branch of solutions with vanishing primary emission.

Since MJD 58238, the ionization degree ($\log \xi$) of the relativistic reflection component is constrained at low values for the majority of the observations (see panel *e* in Fig. 7), suggesting

that the iron line is more likely located at 6.4 keV in the rest frame of the accretion disk (the iron ions are in the form of Fe I – Fe XVII, see House 1969). This result differs from the estimation in Koljonen & Hovatta (2021), wherein relatively high ionization degrees ($\log \xi \geq 3.5$) are obtained.

The accretion disk’s logarithmic electron densities $\log N$ cannot be well-constrained for most of the observations during the decay phase. We obtained a mean value of $\log N \approx 18$ from the best fits (see panel *f* of Fig. 7).

4.2.3. The intensity of the reflection components

Assuming that the emission from the corona is dominant and discarding the branch of solutions with higher $\log \xi$ values, we compute the intensity of each spectral component in our modeling in Eq. 1. The flux ratios between the (non-)relativistic reflection components and the incident primary emission with its 1σ uncertainties are computed and the results are shown in Fig. 10.

We first find that the flux ratio $\mathcal{F}_{\text{xillverCp}}/\mathcal{F}_{\text{Nthcomp}}$ drops rapidly within the first ten days of the decay phase (MJD 58234–58244) and then remain steadily two orders of magnitude weaker than the primary emission for the rest of the time. Assuming the distant reflector remains stable over a 10-day period, the sudden drop in the flux ratio $\mathcal{F}_{\text{xillverCp}}/\mathcal{F}_{\text{Nthcomp}}$ is likely due to the “self-obscuration” of the source, i.e. the radiation from the accretion center was impeded by the thickness of the inner accretion disk. In contrast, the flux ratio $\mathcal{F}_{\text{relxillCp}}/\mathcal{F}_{\text{Nthcomp}}$ continues to decrease after the “self-obscuration” period with this decline lasting until MJD 58280, eventually reaching approximately one-tenth of the primary emission. It maintains this relative strength until the end of the decay phase.

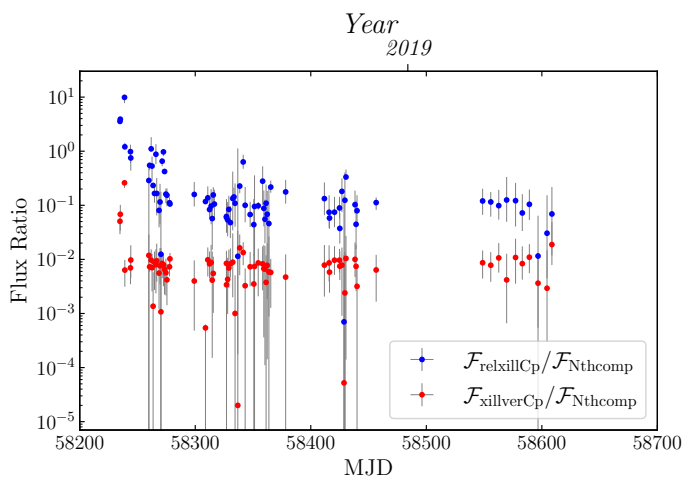


Fig. 10. The evolution of the ratio between the unabsorbed flux of the incident Comptonization spectra and that of the relativistic and distant reflection components versus time. Here we note that the fluxes of *relxillCp*, which models the relativistic reflector, and *xillverCp*, which models the distant reflector, are corrected by the multiplicative model *nthratio* (see Sect. 3.2.2). $\mathcal{F}_{\text{relxillCp}}/\mathcal{F}_{\text{Nthcomp}}$ indicates the geometrical information of the accreting system.

4.2.4. The ionized absorption near the end of the decay phase (MJD 58548–58608)

The emission generated by GRS 1915+105 undergoes a warmly ionized wind absorption near the end of the linear decay (Miller et al. 2020; Koljonen & Hovatta 2021). With the quasi-weekly NICER observations between MJD 58548 and MJD 58608, we can measure the column densities and the ionization degrees of the wind absorption. The results with their 2σ uncertainties are presented in the right part of Fig. 8.

We observe a gradually strengthening absorption column with a slowly decreasing ionization degree $\log \xi$ from ~ 4 to 3 within 60 days. In the last few observations, the complex features between 6.4 keV and 6.7 keV produced by the warm ionized absorber are detected. The highly ionized winds are usually observed in the soft state without QPO features in the time domain (Ponti et al. 2012). However, GRS 1915+105 exhibits strong evidence of a hard-intermediate state at the end of the decay phase, with intermediate Γ values ($2.0 \leq \Gamma \leq 2.4$) and clear type-C QPO signals.

Similar to Sect. 4.1, the launching radius of the wind is calculated with a fixed electron density of 10^{14} cm^{-3} . We thus observe a slightly increasing launching radius with relatively large uncertainties during the end of the decay phase (see panel *c* of Fig. 8) with this fixed electron density. However, we note that the number density of the wind is highly dependent on the radius and the disk polar angle (Fukumura et al. 2017). Thus, the estimation of the launching radius of the wind here is a response to the ionization degree qualitatively, as the unabsorbed luminosity of the source maintains at $\sim 2\% L_{\text{Edd}}$ during the end of the decay phase.

We note that although the model *zxipcf* characterizing the ionized absorption is computed with an incident power-law spectrum of $\Gamma = 2$, which may cause deviation when estimating the ionization degree as the incident spectrum is not a pure power-law with $\Gamma = 2$, the estimated ionization degree $\log \xi$ should not deviate much from the physical value in our study. The uncertainties of $\log \xi$ absorb the systematic errors made by the incident spectrum due to the highly ionized plasma outflowing in

the soft state, and the Γ values do not strongly deviate from 2 at the end of the decay phase.

5. Discussion

5.1. A rarely-seen warm ionized wind in the hard-intermediate state

Since the discovery of the disk winds, the majority of the confirmed ionized wind cases detected in the iron band have been found in the soft state of the BHBs and with a high ionization degree ($\log \xi \geq 4$) (see e.g., Miller et al. 2006a,b; Kubota et al. 2007; Neilsen & Lee 2009; Ponti et al. 2012). Although there are several reports on the ionized absorption observed in the hard or hard-intermediate state, some of the detections depend on the choice of the reflection models (Xu et al. 2018; Wang et al. 2021). Lee et al. (2002) reported a highly ionized wind ($\log \xi \simeq 4.15$) in GRS 1915+105 when the source was in the hard χ state, but the unabsorbed luminosity of the source reached $\sim 40\% L_{\text{Edd}}$ at that time. It is natural to produce a highly ionized wind with such a high luminosity. Shidatsu et al. (2013) detected a warmly ionized wind in the hard state of MAXI J1305–704, with the ionization degree of $\log \xi \sim 2$.

The behaviors of the absorber are dependent on the assumptions. With a variable electron density by assuming that the thickness of the wind ΔR is comparable to the launching radius R_{launch} , the electron density N_e can be estimated by $N_e = N_{\text{H}}/\Delta R \sim N_{\text{H}}/R_{\text{launch}}$. Therefore, $R_{\text{launch}} \sim L/(N_{\text{H}} \cdot \xi)$. The mean value of the estimated N_e at the end of the decay is about 10^{13} cm^{-3} , which will not result in a change of R_{launch} by more than one order of magnitude. Rather, with a constant N_e of 10^{14} cm^{-3} , the estimated R_{launch} of the absorber shows a potentially extremely-slow outward movement with an upper limit of speed of $\dot{R}_{\text{launch}} \simeq 0.02 \text{ km} \cdot \text{s}^{-1}$. Compared with the velocity of the wind itself ($v \geq 10^2 \text{ km} \cdot \text{s}^{-1}$, see Miller et al. 2020), the motion of the launching radius is negligible.

The estimated launching radii of the winds in GRS 1915+105 during the soft state before 2018 and the end of the decay phase in 2019 are both in the range of 10^3 – $10^4 r_g$, which suggests that the launching mechanism of the outflow is likely the same. Although the obscuration of this source after May 2019 is attributed to local absorption (Neilsen et al. 2020; Balakrishnan et al. 2021), the cause of the decay before the obscuration is different. The neutral absorption $N_{\text{H, neutral}}$ maintains at $6 \times 10^{22} \text{ cm}^{-2}$ throughout the decay, not showing significant enhancement until the onset of the obscured state. The cold matter seen in the obscured state likely originates from the outflow formed near the end of the decay.

5.2. The interaction between the corona and the accretion disk

In Sect. 4.2.3 we presented the intensity analysis between the primary emission and the (non-)relativistic reflection components (see Fig. 10). The ratio $\mathcal{F}_{\text{relxillCp}}/\mathcal{F}_{\text{Nthcomp}}$ and $\mathcal{F}_{\text{xillverCp}}/\mathcal{F}_{\text{Nthcomp}}$ may unveil the geometrical information of the accreting system.

Both $\mathcal{F}_{\text{relxillCp}}/\mathcal{F}_{\text{Nthcomp}}$ and $\mathcal{F}_{\text{xillverCp}}/\mathcal{F}_{\text{Nthcomp}}$ drop to one-tenth of their original values during the first ten days of the decay phase (MJD 58234–58244). These drastic decreases are likely produced by the fading of the self-obscuration of the accreting system. $\mathcal{F}_{\text{xillverCp}}/\mathcal{F}_{\text{Nthcomp}}$ holds steady at 10^{-2} after the 10-day period, but $\mathcal{F}_{\text{relxillCp}}/\mathcal{F}_{\text{Nthcomp}}$ continues to decrease from 10^0 to 10^{-1} in the following 30 days (MJD 58245–58275). The decrease observed solely in $\mathcal{F}_{\text{relxillCp}}/\mathcal{F}_{\text{Nthcomp}}$ is likely associated

with the geometrical changes of the accreting system during an intermediate-to-hard transition.

It has been found that in BHBs in general the reflection component becomes stronger when the spectrum is softer due to weaker Comptonization in soft states (Steiner et al. 2016). Therefore, the ratio $\mathcal{F}_{\text{relxillCp}}/\mathcal{F}_{\text{Nthcomp}}$ is assumed to become smaller in the intermediate-to-hard transition and vice versa. Although the states exhibited by GRS 1915+105 are generally not strictly the canonical hard or soft states during an outburst, it can still undergo transitions that are considered part of the canonical state evolution due to the long-term instability of the corona. Similar incomplete transitions have also been found in other persistent sources, e.g., Cyg X-1 (Zhou et al. 2022). The reduction in the flux ratio at the beginning of the decay phase aligns with this expectation. We expect to observe an increase of this ratio at the end of the decay phase if the latter transition is normal, as both the photon indices Γ and the frequencies of the QPO increase then. However, the flux ratio remains low and even exhibits a decreasing trend till the end of the decay phase, which suggests that the transition near the end of the decay phase is different from a normal softening state transition.

In the context of the lamp-post model in which the corona is simplified as a point-like source above the disk, the two ratios can be easily interpreted as signals of the distances between the corona and two different reflectors. An increasing ratio means a closer distance and vice versa. The evolution of $\mathcal{F}_{\text{relxillCp}}/\mathcal{F}_{\text{Nthcomp}}$ suggests that the corona is consistently receding from the accretion disk in this scenario. However, recent polarization results indicate that the primary photon emitter could be parallel to the accretion disk rather than a source hanging perpendicular to the accretion disk (Krawczynski et al. 2022; Veldina et al. 2023; however, see e.g., Dexter & Begelman 2024 for a different interpretation). In the according scenario, the ratio $\mathcal{F}_{\text{relxillCp}}/\mathcal{F}_{\text{Nthcomp}}$ works as an indicator of the strength of the interaction between the corona and the standard accretion disk. In the normal hard state, the optical depth of the corona is higher, resulting in more photons being scattered and diluting the initial relativistic effects of the disk photons (Petrucci et al. 2001). In contrast, the source exhibits weak interaction at the end of the decay phase. This odd phenomenon might be attributed to the changed geometry of the accretion system, for instance, a relatively shrinking standard disk due to the lack of infalling material. Returning radiation can also play an important role in producing reflection components (Mirzaev et al. 2024). The photons emitted from the inner part of the disk have a higher probability of arriving at the surface of the accretion disk and re-irradiating the disk again (Dauser et al. 2022). An increasing inner radius of the disk during this period can weaken the irradiation from the returning radiation and thus reduce the flux of the relativistic reflection component.

5.3. The interplay between the disk winds and the corona during and after the decay

The physical mechanisms in the accretion process of BHBs are still debated, but we benefit from observational evidence to gradually disentangle the puzzle of accretion. The jets and disk winds usually exhibit mutually exclusive interplay within a normal outburst (Neilsen & Lee 2009; Ponti et al. 2012), although exceptions exist (Miller et al. 2006b; Kalemci et al. 2016; Homan et al. 2016; Motta et al. 2021). The behaviors of the jet are considered closely related to the corona (see e.g., Markoff et al. 2005).

In GRS 1915+105, we have confirmed that the source underwent a partially hardening-to-softening transition during the

decay phase, where the ionized wind absorption features merely appear near the end of the decay. Type-C QPOs are detected throughout the decay phase and their frequencies are strongly correlated to the photon indices of the Comptonization component. The spectral-timing behaviors of the corona seem independent from the emergence of the ionized disk outflow.

Assuming the disk winds observed in both the soft state and the hard decay phase share the same launching mechanism, forcibly linking the appearance of disk wind with the vanishing of the jet or the softening of the spectrum will lead to irreconcilable contradictions. The radio emission and the disk wind clearly co-exist during the end of the decay phase (Motta et al. 2021). It is also not very feasible to connect the appearance of disk winds with the movement of r_{in} , the inner radius of the disk, as r_{in} approaches the ISCO in the soft state but increases in the scenario of returning radiation. However, considering that the wind's launching position is far from the binary center, a potential hysteretic interaction between the corona and the periphery of the accretion disk can be suggested. Typically, suppressed jets release less energy into the environment, with more energy directed towards Compton heating, which accelerates the winds (Narayan & Yi 1995; Merloni & Fabian 2002). These winds carry away angular momentum, slowing the mass inflow and promoting faster thermal equilibrium in the inner regions of the accretion disk (Blandford & Begelman 1999). However, during the decay phase of GRS 1915+105, winds driven by relatively low luminosity would further decelerate the in-falling matter, leading to a more rapid fading of the accretion system and eventually resulting in the emergence of the obscured state.

Neilsen et al. (2020) reported a fast flare observed in the obscured state of GRS 1915+105. Fe xxvi Ly α and Fe xxv He α lines were detected in emission before the flare and in absorption when the count rate increased, indicating that the highly ionized outflow always existed during the focused observation: absorption lines are visible when a strong central source backlights the medium, and emission lines emerge when the central source becomes faint. In the periods with a lower count rate, three prominent emission lines (quasi-neutral Fe K α line at 6.4 keV, Fe xxv He α line at 6.7 keV, and Fe xxvi Ly α at 7 keV) are observed (Miller et al. 2020; Koljonen & Hovatta 2021) in the Fe band. The origins of the three lines are different, as the quasi-neutral Fe lines come from the cooling area of the accretion disk and the ionized Fe lines come from the highly ionized plasma flowing outward the disk. The emergence of three Fe emission lines is not unique to GRS 1915+105, and has been found in other systems such as V404 Cygni (King et al. 2015) and V4641 Sgr (Shaw et al. 2022), which are well-known for their high inclination and variable local obscuration (Koljonen & Tomsick 2020).

6. Conclusions

We have conducted spectral-timing analysis of GRS 1915+105, utilizing all available NICER and Insight–HXMT data before MJD 58617 when the source entered into the obscured state. In particular, we used simultaneous NICER and HXMT data to develop a model that described the broadband spectrum of the source and used this model with the higher-cadence NICER data to trace the evolution of the source.

In the disk-dominated state before 2018, we consistently observe a highly ionized wind with the detection of the Fe xxvi Ly α line at 7 keV. The photon index approaches the upper limit of our model ($\Gamma \approx 3.4$), and the intensity of the thermal radiation dominates the spectrum.

During the decay phase corresponding to a spectral transition from a partially hardening process to an unusual obscuring process, we have found a quasi-linear correlation between the photon index Γ and the frequency of the main QPO with both an empirical model and an improved physical model. At the end of the decay phase, the spectrum shows strong absorption features with a decreasing ionization degree when the source was in the hard-intermediate state with clear type-C QPO features. The estimated launching radius of this warmly ionized outflow appears to be the same order of magnitude as that in the soft state, indicating that the launching mechanism of the winds is likely the same in both the soft state and the hard state near the end of the decay.

At the beginning of the decay phase, the relative intensity of both the relativistic and non-relativistic reflection components is strong but weakens by a factor of 10 within 10 days, possibly due to the vanishing of self-obscuration in the accreting system. The relativistic reflection component continues to weaken over the next 30 days, while the non-relativistic reflection component remains steady. Both reflection components maintain their relative strengths in the middle of the decay phase. However, the relativistic component even shows a potentially decreasing trend as warmly ionized winds appear near the end of the decay. This discrepancy corresponds to an unusual softening process, indicating either an increasing distance between the disk and the corona (in the context of the lamp-post model) or a rising inner radius of the disk (in the context of returning radiation). The QPO frequencies and photon index are strongly interdependent, with the launch of ionized winds further slowing the accreting of the infalling matter.

Acknowledgements. M. Z. would like to thank the support from the China Scholarship Council (CSC 202006100027). This research has made use of NASA's Astrophysics Data System Bibliographic Services. This research also made use of ISIS functions (`isiscripts`³) provided by ECAP/Remeis observatory and MIT. This work made use of data from the Insight-HXMT mission, a project funded by the China National Space Administration (CNSA) and the Chinese Academy of Sciences (CAS). L. D. Kong is grateful for the financial support provided by the Sino-German (CSC-DAAD) Postdoc Scholarship Program (57607866).

References

Arnaud, K. A. 1996, in *Astronomical Society of the Pacific Conference Series*, Vol. 101, *Astronomical Data Analysis Software and Systems V*, ed. G. H. Jacoby & J. Barnes, 17

Athulya, M. P., Radhika, D., Agrawal, V. K., et al. 2022, *MNRAS*, 510, 3019

Bachetti, M., Huppenkothen, D., Khan, U., et al. 2021, *StingraySoftware/stingray: Version 0.3*

Balakrishnan, M., Miller, J. M., Reynolds, M. T., et al. 2021, *ApJ*, 909, 41

Bardeen, J. M. & Petterson, J. A. 1975, *ApJ*, 195, L65

Begelman, M. C., McKee, C. F., & Shields, G. A. 1983, *ApJ*, 271, 70

Belloni, T., Klein-Wolt, M., Méndez, M., van der Klis, M., & van Paradijs, J. 2000, *A&A*, 355, 271

Blandford, R. D. & Begelman, M. C. 1999, *MNRAS*, 303, L1

Böck, M., Grinberg, V., Pottschmidt, K., et al. 2011, *A&A*, 533, A8

Bogdanov, S., Guillot, S., Ray, P. S., et al. 2019, *ApJ*, 887, L25

Cao, X., Jiang, W., Meng, B., et al. 2020, *Science China Physics, Mechanics, and Astronomy*, 63, 249504

Castro-Tirado, A. J., Brandt, S., & Lund, N. 1992, *IAU Circ.*, 5590, 2

Castro-Tirado, A. J., Brandt, S., Lund, N., et al. 1994, *ApJS*, 92, 469

Chen, Y., Cui, W., Li, W., et al. 2020, *Science China Physics, Mechanics, and Astronomy*, 63, 249505

Dauser, T., García, J., Parker, M. L., Fabian, A. C., & Wilms, J. 2014, *MNRAS*, 444, L100

Dauser, T., García, J. A., Joyce, A., et al. 2022, *MNRAS*, 514, 3965

Dexter, J. & Begelman, M. C. 2024, *MNRAS*, 528, L157

Done, C., Tomaru, R., & Takahashi, T. 2018, *MNRAS*, 473, 838

³ <http://www.sternwarte.uni-erlangen.de/isis/>

Fender, R. P., Garrington, S. T., McKay, D. J., et al. 1999, *MNRAS*, 304, 865

Fender, R. P., Stirling, A. M., Spencer, R. E., et al. 2006, *MNRAS*, 369, 603

Fukumura, K., Kazanas, D., Shrader, C., et al. 2017, *Nature Astronomy*, 1, 0062

García, J., Dauser, T., Lohfink, A., et al. 2014, *ApJ*, 782, 76

García, J., Dauser, T., Reynolds, C. S., et al. 2013, *ApJ*, 768, 146

Gendreau, K. C., Arzoumanian, Z., Adkins, P. W., et al. 2016, in *Society of Photo-Optical Instrumentation Engineers (SPIE) Conference Series*, Vol. 9905, *Space Telescopes and Instrumentation 2016: Ultraviolet to Gamma Ray*, ed. J.-W. A. den Herder, T. Takahashi, & M. Bautz, 99051H

Grevesse, N., Noels, A., Sauval, A., Holt, S., & Sonneborn, G. 1996, in *ASP Conf. Ser.*, Vol. 99, 117

Grinberg, V., Pottschmidt, K., Böck, M., et al. 2014, *A&A*, 565, A1

Guo, C.-C., Liao, J.-Y., Zhang, S., et al. 2020, *Journal of High Energy Astrophysics*, 27, 44

Hannikainen, D. C., Rodriguez, J., Vilhu, O., et al. 2005, *A&A*, 435, 995

Higginbottom, N. & Proga, D. 2015, *ApJ*, 807, 107

Homan, J., Neilsen, J., Allen, J. L., et al. 2016, *ApJ*, 830, L5

Homan, J., Neilsen, J., Steiner, J., et al. 2019, *The Astronomer's Telegram*, 12742, 1

Homan, J., Wijnands, R., van der Klis, M., et al. 2001, *ApJS*, 132, 377

Houck, J. C. & Denicola, L. A. 2000, in *Astronomical Society of the Pacific Conference Series*, Vol. 216, *Astronomical Data Analysis Software and Systems IX*, ed. N. Manset, C. Veillet, & D. Crabtree, 591

House, L. L. 1969, *ApJS*, 18, 21

Huppenkothen, D., Bachetti, M., Stevens, A., et al. 2019a, *The Journal of Open Source Software*, 4, 1393

Huppenkothen, D., Bachetti, M., Stevens, A. L., et al. 2019b, *ApJ*, 881, 39

Ingram, A. & Done, C. 2011, *MNRAS*, 415, 2323

Ingram, A., Done, C., & Fragile, P. C. 2009, *MNRAS*, 397, L101

Kaastra, J. S. & Bleeker, J. A. M. 2016, *A&A*, 587, A151

Kalemcı, E., Begelman, M. C., Maccarone, T. J., et al. 2016, *MNRAS*, 463, 615

Kallman, T. R., Palmeri, P., Bautista, M. A., Mendoza, C., & Krolik, J. H. 2004, *ApJS*, 155, 675

King, A. L., Miller, J. M., Raymond, J., Reynolds, M. T., & Morningstar, W. 2015, *ApJ*, 813, L37

Klein-Wolt, M., Fender, R. P., Pooley, G. G., et al. 2002, *MNRAS*, 331, 745

Koljonen, K., Vera, R., Lahteenmaki, A., & Tornikoski, M. 2019, *The Astronomer's Telegram*, 12839, 1

Koljonen, K. I. I. & Hovatta, T. 2021, *A&A*, 647, A173

Koljonen, K. I. I. & Tomsick, J. A. 2020, *A&A*, 639, A13

Kong, L.-D., Ji, L., Santangelo, A., et al. 2024, *A&A*, 686, A211

Kong, L. D., Zhang, S., Chen, Y. P., et al. 2021, *ApJ*, 906, L2

Krawczynski, H., Muleri, F., Dovčiak, M., et al. 2022, *Science*, 378, 650

Kubota, A., Dotani, T., Cottam, J., et al. 2007, *PASJ*, 59, 185

Lee, J. C., Reynolds, C. S., Remillard, R., et al. 2002, *ApJ*, 567, 1102

Li, X., Li, X., Tan, Y., et al. 2020, *Journal of High Energy Astrophysics*, 27, 64

Liao, J.-Y., Zhang, S., Chen, Y., et al. 2020a, *Journal of High Energy Astrophysics*, 27, 24

Liao, J.-Y., Zhang, S., Lu, X.-F., et al. 2020b, *Journal of High Energy Astrophysics*, 27, 14

Liu, C., Zhang, Y., Li, X., et al. 2020, *Science China Physics, Mechanics, and Astronomy*, 63, 249503

Makishima, K., Maejima, Y., Mitsuda, K., et al. 1986, *ApJ*, 308, 635

Markoff, S., Nowak, M. A., & Wilms, J. 2005, *ApJ*, 635, 1203

Martocchia, A., Matt, G., Belloni, T., et al. 2006, *A&A*, 448, 677

Matsuoka, M., Kawasaki, K., Ueno, S., et al. 2009, *PASJ*, 61, 999

Matt, G., Guainazzi, M., & Maiolino, R. 2003, *MNRAS*, 342, 422

Merloni, A. & Fabian, A. C. 2002, *MNRAS*, 332, 165

Miller, J. M., Parker, M. L., Fuerst, F., et al. 2013, *ApJ*, 775, L45

Miller, J. M., Raymond, J., Fabian, A., et al. 2006a, *Nature*, 441, 953

Miller, J. M., Raymond, J., Fabian, A. C., et al. 2016, *ApJ*, 821, L9

Miller, J. M., Raymond, J., Homan, J., et al. 2006b, *ApJ*, 646, 394

Miller, J. M., Zoghbi, A., Raymond, J., et al. 2020, *ApJ*, 904, 30

Mirabel, I. F. & Rodríguez, L. F. 1994, *Nature*, 371, 46

Mirzaev, T., Riaz, S., Abdikamalov, A. B., et al. 2024, *ApJ*, 965, 66

Mitsuda, K., Inoue, H., Koyama, K., et al. 1984, *PASJ*, 36, 741

Morgan, E. H., Remillard, R. A., & Greiner, J. 1997, *ApJ*, 482, 993

Motta, S., Muñoz-Darias, T., Casella, P., Belloni, T., & Homan, J. 2011, *MNRAS*, 418, 2292

Motta, S., Williams, D., Fender, R., et al. 2019, *The Astronomer's Telegram*, 12773, 1

Motta, S. E., Kajava, J. J. E., Giustini, M., et al. 2021, *MNRAS*, 503, 152

Motta, S. E., Kajava, J. J. E., Sánchez-Fernández, C., et al. 2017a, *MNRAS*, 471, 1797

Motta, S. E., Kajava, J. J. E., Sánchez-Fernández, C., Giustini, M., & Kuulkers, E. 2017b, *MNRAS*, 468, 981

Narayan, R. & Yi, I. 1995, *ApJ*, 444, 231

Negoro, H., Tachibana, Y., Kawai, N., et al. 2018, *The Astronomer's Telegram*, 11828, 1

Neilsen, J., Cackett, E., Remillard, R. A., et al. 2018, *ApJ*, 860, L19

- Neilsen, J., Homan, J., Steiner, J. F., et al. 2020, *ApJ*, 902, 152
- Neilsen, J. & Lee, J. C. 2009, *Nature*, 458, 481
- Nowak, M. A. 2000, *MNRAS*, 318, 361
- Petrucci, P. O., Merloni, A., Fabian, A., Haardt, F., & Gallo, E. 2001, *MNRAS*, 328, 501
- Ponti, G., Fender, R. P., Begelman, M. C., et al. 2012, *MNRAS*, 422, L11
- Proga, D. & Kallman, T. R. 2002, *ApJ*, 565, 455
- Reeves, J., Done, C., Pounds, K., et al. 2008, *MNRAS*, 385, L108
- Reid, M. J., McClintock, J. E., Steiner, J. F., et al. 2014, *ApJ*, 796, 2
- Remillard, R. A., Loewenstein, M., Steiner, J. F., et al. 2022, *AJ*, 163, 130
- Remillard, R. A. & McClintock, J. E. 2006, *ARA&A*, 44, 49
- Remillard, R. A., Morgan, E. H., McClintock, J. E., Bailyn, C. D., & Orosz, J. A. 1999, *ApJ*, 522, 397
- Shaw, A. W., Miller, J. M., Grinberg, V., et al. 2022, *MNRAS*, 516, 124
- Shi, Z., Wu, Q., Yan, Z., Lyu, B., & Liu, H. 2023, *MNRAS*, 525, 1431
- Shidatsu, M., Ueda, Y., Nakahira, S., et al. 2013, *ApJ*, 779, 26
- Shreeram, S. & Ingram, A. 2020, *MNRAS*, 492, 405
- Soleri, P., Belloni, T., & Casella, P. 2008, *MNRAS*, 383, 1089
- Steiner, J. F., Remillard, R. A., García, J. A., & McClintock, J. E. 2016, *ApJ*, 829, L22
- Tagger, M. & Pellat, R. 1999, *A&A*, 349, 1003
- Tarter, C. B., Tucker, W. H., & Salpeter, E. E. 1969, *ApJ*, 156, 943
- Tomsick, J. A. & Kaaret, P. 2000, *ApJ*, 537, 448
- Ueda, Y., Yamaoka, K., & Remillard, R. 2009, *ApJ*, 695, 888
- Veledina, A., Muleri, F., Dovčiak, M., et al. 2023, *ApJ*, 958, L16
- Verner, D. A., Ferland, G. J., Korista, K. T., & Yakovlev, D. G. 1996, *ApJ*, 465, 487
- Wang, Y., Ji, L., García, J. A., et al. 2021, *ApJ*, 906, 11
- Williams, D. R. A., Motta, S. E., Fender, R., et al. 2020, *MNRAS*, 491, L29
- Wilms, J., Allen, A., & McCray, R. 2000, *ApJ*, 542, 914
- Woods, D. T., Klein, R. I., Castor, J. I., McKee, C. F., & Bell, J. B. 1996, *ApJ*, 461, 767
- Xu, Y., Harrison, F. A., Kennea, J. A., et al. 2018, *ApJ*, 865, 18
- Zdziarski, A. A., Gierliński, M., Mikołajewska, J., et al. 2004, *MNRAS*, 351, 791
- Zdziarski, A. A., Johnson, W. N., & Magdziarz, P. 1996, *MNRAS*, 283, 193
- Zhang, S., Lu, F. J., Zhang, S. N., & Li, T. P. 2014, in *Society of Photo-Optical Instrumentation Engineers (SPIE) Conference Series*, Vol. 9144, *Space Telescopes and Instrumentation 2014: Ultraviolet to Gamma Ray*, ed. T. Takahashi, J.-W. A. den Herder, & M. Bautz, 914421
- Zhang, S.-N., Li, T., Lu, F., et al. 2020, *Science China Physics, Mechanics, and Astronomy*, 63, 249502
- Zhang, W., Jahoda, K., Swank, J. H., Morgan, E. H., & Giles, A. B. 1995, *ApJ*, 449, 930
- Zhou, M., Grinberg, V., Bu, Q. C., et al. 2022, *A&A*, 666, A172
- Zoghbi, A., Miller, J. M., King, A. L., et al. 2016, *ApJ*, 833, 165
- Życki, P. T., Done, C., & Smith, D. A. 1999, *MNRAS*, 309, 561